Vol 465|27 May 2010|doi:10.1038/nature09001

LETTERS

Embolus extravasation is an alternative mechanism for cerebral microvascular recanalization

Carson K. Lam[1]*, Taehwan Yoo[1]*, Bennett Hiner[1], Zhiqiang Liu[1] & Jaime Grutzendler[1,2]

Cerebral microvascular occlusion is a common phenomenon throughout life[1,2] that might require greater recognition as a mechanism of brain pathology. Failure to recanalize microvessels promptly may lead to the disruption of brain circuits and significant functional deficits[3]. Haemodynamic forces and the fibrinolytic system[4] are considered to be the principal mechanisms responsible for recanalization of occluded cerebral capillaries and terminal arterioles. Here we identify a previously unrecognized cellular mechanism that may also be critical for this recanalization. By using high-resolution fixed-tissue microscopy and two-photon imaging in living mice we observed that a large fraction of microemboli infused through the internal carotid artery failed to be lysed or washed out within 48 h. Instead, emboli were found to translocate outside the vessel lumen within 2–7 days, leading to complete re-establishment of blood flow and sparing of the vessel. Recanalization occurred by a previously unknown mechanism of microvascular plasticity involving the rapid envelopment of emboli by endothelial membrane projections that subsequently form a new vessel wall. This was followed by the formation of an endothelial opening through which emboli translocated into the perivascular parenchyma. The rate of embolus extravasation was significantly decreased by pharmacological inhibition of matrix metalloproteinase 2/9 activity. In aged mice, extravasation was markedly delayed, resulting in persistent tissue hypoxia, synaptic damage and cell death. Alterations in the efficiency of the protective mechanism that we have identified may have important implications in microvascular pathology, stroke recovery and age-related cognitive decline.

Cerebral function and viability are dependent on uninterrupted blood flow through the microvasculature for the adequate delivery of oxygen and glucose[5]. Thus, robust mechanisms must have evolved to ensure microvascular patency. The fibrinolytic system provides the principal mechanism for the degradation of blood clots occluding cerebral blood vessels[4], including terminal arterioles and capillaries[6,7]. As a result of their small diameter and relatively low flow velocity, microvessels may be prone to occlusion by spontaneously formed microclots and by debris that are not susceptible to fibrinolysis, such as fragments of atheromatous plaques[8]. It is not known whether and how blood flow is re-established when haemodynamic forces and the fibrinolytic system fail to clear occluded microvessels.

To address these questions, we developed a set of tools to reveal the outcome of individual occlusions of capillaries and terminal arterioles in the mouse brain. Transcranial imaging in living mice with two-photon microscopy (TPM)[9] and high-resolution confocal and electron microscopy was performed after internal carotid infusion of fluorescently conjugated microemboli (8–20 μm). Although a substantial number of emboli were cleared within 2 h after infusion, presumably by a combined effect of the fibrinolytic system and haemodynamic forces (Supplementary Figs 2 and 12), many emboli remained in the microvasculature (Fig. 1f) and only a modest number were washed out thereafter (Fig. 1g). Thus, although fibrinolysis and haemodynamic forces are effective in the early clearance of emboli, their efficiency is much lower at later stages. Once retained in the microvasculature, emboli generally caused a cessation of blood flow as demonstrated by the absence of the characteristic pattern of flowing cells observed in line-scan imaging (Fig. 1d, day 1, and Supplementary Movie 5).

To determine the outcome of these persistent vessel occlusions, we extended our imaging intervals. As early as 2 days after embolization we observed that many emboli no longer seemed to be located in the interior of the blood vessels, and by day 6 most had translocated outside the vessel lumen (Fig. 1a–d, h) re-establishing blood flow (Fig. 1d, days 3 and 5, and Supplementary Movie 2). Given the gradual nature of the extravasation process, it was not possible to image the precise instant of recanalization. However, regardless of when extravasation occurred, in every imaging session in which we saw completely extravasated emboli, flow was already present at the time of imaging (34 out of 34 extravasated fibrin emboli at 2, 3, 5 and 8 days after embolization), suggesting that vessel reflow occurred rapidly. Furthermore, in larger microvessels (about 20 μm), which allow the flow of multiple rows of cells, reflow was observed even before complete extravasation of the embolus (Fig. 1e, Supplementary Figs 3 and 4 and Supplementary Movie 4).

The extravasation phenomenon was observed with fibrin clots (Fig, 1a, b, d) and with substances not susceptible to fibrinolysis such as cholesterol emboli (Figs 1c and 2a) and polystyrene microspheres (Fig. 1k and Supplementary Movie 3). *In vivo* imaging in mice expressing endothelial-specific green fluorescent protein (Tie2–GFP) demonstrated the extravascular location of emboli (Figs 1a–c and 2a–d). This was further confirmed by confocal imaging in tissues immunolabelled for platelet–endothelial cell adhesion molecule-1 (PECAM-1) and extracellular matrix protein collagen IV (Supplementary Fig. 6). Transmission electron microscopy demonstrated fibrin clots and microspheres outside the microvascular lumen and surrounded by processes of perivascular cells (Fig. 1i–k). The pattern of clot extravasation was variable: fibrin clots had a tendency to extravasate in smaller fragments (about 3–10 μm) (Fig. 1d) although many times in larger pieces (Figs 1a, b), whereas cholesterol emboli generally extravasated with minimal fragmentation (Figs 1c and 2a).

Several mechanisms could explain the translocation of embolic material outside the vessel lumen. One possibility is that it occurs by mechanisms similar to the translocation of leukocytes through the blood–brain barrier[10,11]. Alternatively, endothelial cells near the occlusion may degenerate, allowing the passage of embolic fragments through the vessel, which is then repaired by endothelial proliferation. However, this was ruled out by the absence of immunolabelling

[1]Department of Neurology, Northwestern University Feinberg School of Medicine, Chicago, Ilinois 60611 USA. [2]Physiology, Northwestern University Feinberg School of Medicine, Chicago, Ilinois 60611, USA.
*These authors contributed equally to this work.

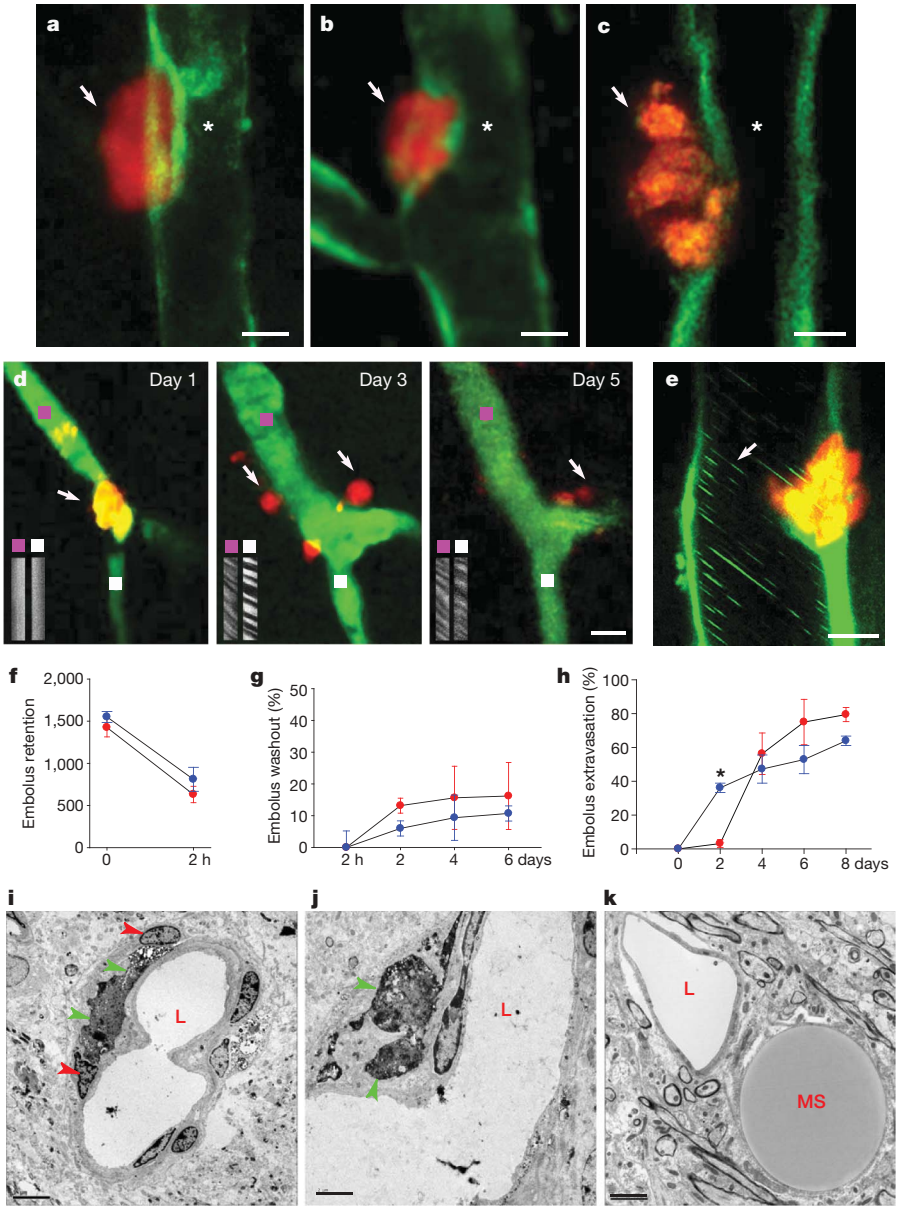

Figure 1 | Emboli that fail to be washed out undergo extravasation leading to re-establishment of blood flow. a–c, Single-time-point transcranial TPM imaging in Tie2–GFP mice show extravasated fluorescent fibrin clots (arrows in **a** and **b**; day 4 after embolization) and a cholesterol embolus (arrow in **c**; day 3 after embolization) adjacent to recanalized lumen (asterisk). Different clot sizes are shown in **a** and **b**. Scale bars, 10 μm. **d**, Time-lapse imaging shows a capillary (green; intravascular thioflavin-S dye) occluded by a fibrin clot (orange; arrow, day 1), which extravasates and degrades (arrows, days 3 and 5; Supplementary Fig. 11). Line-scan imaging upstream (purple squares) and downstream (white squares) of the occlusion shows blood flow re-establishment. **e**, *In vivo* image on day 2 shows a cholesterol embolus in the process of extravasation through the GFP-labelled endothelium (ACTB–eGFP mice). Leukocytes (green lines, arrow) are seen flowing even before complete extravasation. **f**, Quantification of fibrin (red points) and cholesterol (blue points) emboli (10–20 μm) retained in the microvasculature that failed to be lysed or washed out 2 h after embolization (about 1,500 clots per mouse in 12 mice; means ± s.e.m.). **g**, Fibrin and cholesterol emboli washout up to 6 days after embolization (means ± s.e.m.; $n = 3$ mice per time point). **h**, Fibrin and cholesterol emboli extravasation up to 8 days after embolization (means ± s.e.m.; $n = 10$ mice and 17 fibrin clots and $n = 10$ mice and 18 cholesterol emboli per mouse). The difference in early extravasation rates between cholesterol and clots (asterisk, $P < 0.01$) is probably due to a tendency of clots to dislodge from their initial site of occlusion. **i–k**, Transmission electron microscopy shows colloidal carbon-conjugated fibrin clots (**i**, **j**, green arrowheads) that have extravasated after 7 days and are surrounded by the processes of perivascular cells (red arrowheads), and (**k**) a microsphere (MS) outside the capillary lumen (L). Different clot sizes are shown in **i** and **j**. Scale bars, 5 μm.

with the cell death marker caspase-3 (0 out of 35 occluded microvessels in three mice) or the proliferation marker bromodeoxyuridine (BrdU) (0 out of 73 occluded vessels in seven mice).

To determine the precise cellular events involved in embolus extravasation, we obtained *in vivo* time-lapse images of fibrin and cholesterol emboli as they underwent extravasation in Tie2–GFP mice. To our surprise, regardless of the composition of the embolic material, we found that within 24–48 h the endothelium generated membrane projections that completely enveloped the adjacent emboli (Fig. 2a–d, Supplementary Movie 1 and Supplementary Fig. 13). In some cases the new endothelial membrane was in close contact with the opposing endothelium (Fig. 2c, day 3), whereas in others they seemed to form a narrow lumen (Fig. 2d, day 3). Transmission electron microscopy confirmed the presence of endothelial membrane projections covering entire emboli (Fig. 2e–j), which in some cases were found in contact with the opposing endothelium (Fig. 2e, g) forming cell–cell adhesion structures (Fig. 2f, h) resembling adherens junctions[12]. In other cases, endothelial membranes seemed separate from each other, forming a proto-lumen (Fig. 2i, j) similar to their appearance under *in vivo* imaging (Fig. 2a, b, d). This suggests a sequence of

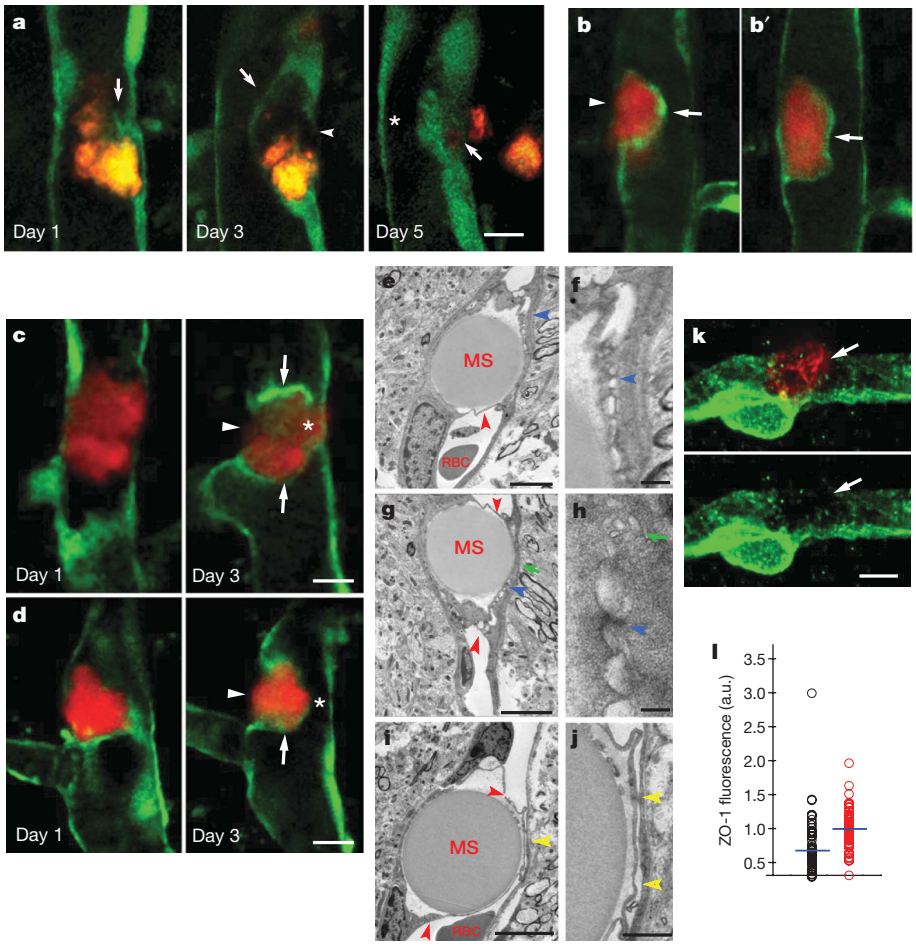

Figure 2 | Focal endothelial remodelling underlies the translocation of emboli. a, Time-lapse imaging in Tie2–GFP mice shows the gradual extension of a membrane from the adjacent endothelium (arrow, day 1) eventually surrounding a cholesterol embolus (orange) (arrow, day 3). The original endothelium undergoes retraction (arrowhead, day 3) creating a path for embolus translocation. On day 5 the embolus has extravasated, leading to lumen recanalization (asterisk). **b**, **b′**, Single-time-point *in vivo* image shows two optical planes of the same vessel. The fibrin clot (red) is enveloped by a newly formed endothelial extension (arrow) and an opening in the endothelium is visible through which the clot seems to be extravasating (arrowhead in **b**) (Supplementary Movie 1). **c**, **d**, Time-lapse images in Tie2–GFP mice show fibrin clots (red) at different stages in the formation of the endothelial envelope (arrows), endothelial retraction (arrowheads) and lumen re-establishment (asterisks). **e**–**j**, Transmission electron microscopy shows intravascular microspheres that have been enveloped by endothelial extensions (red arrowheads). The newly formed membranes make contact with the opposing endothelium forming specialized cellular junctions (blue arrowheads in **e**–**h**) and small vacuolar structures (green arrows in **g** and **h**). **i**, **j**, Endothelial membranes are detached from each other and a narrow lumen is apparent (yellow arrowheads). RBC, red blood cell. **k**, Confocal image of a microvessel immunolabelled for ZO-1 (green) shows decreased labelling (arrow in lower panel) adjacent to an intravascular fibrin clot (red, arrow in upper panel). In the bottom panel the red channel is cancelled to allow visualization of the green channel near the clot. Scale bar, 10 μm. **l**, Quantification of ZO-1 immunofluorescence adjacent to clots (black points) and control unoccluded microvessels (red points) in the same confocal optical plane ($n = 5$ mice and 55 and 57 vessels, $P < 0.001$, two-sided Mann–Whitney test).

events in which the newly formed endothelial membranes frequently make transient adhesion with the opposing endothelium. This is followed by gradual separation after the dissociation of cell–cell junctions and possibly by the formation of coalescing endothelial vesicles (Fig. 2h) in a similar manner to the process that occurs during lumen formation in the developing vasculature[13]. Transient cell adhesion may help in guiding the movement of the endothelial membrane projections while minimizing pathological plasma leakage during extravasation.

Once emboli have been enveloped, their final movement into the parenchyma requires disruption of the original endothelium to allow their passage. *In vivo* imaging in Tie2–GFP mice demonstrated that during the formation of membrane projections the original endothelium undergoes remodelling in what seems to be a retraction process (Fig. 2a–d), creating a path for embolus translocation (Fig. 2a). However, it is not clear whether these endothelial changes are due to the formation of a large transcellular channel or whether they occur by disruption of interendothelial tight junctions, both of which have been proposed as mechanisms of leukocyte transmigration[10,11,14]. Given that the amount of tight-junction protein zonula occludens-1 (ZO-1) is decreased in microvascular areas adjacent to clots (Fig. 2k, l), tight-junction disruption may be involved in the final endothelial breach before extravasation. Although it is not clear what forces drive the final extrusion of emboli, both haemodynamic pressure and focal microvascular constriction mediated by pericytes[15] could be involved, given that we find increased pericyte NG2 immunofluorescence near emboli (Supplementary Fig. 7).

In addition to extravasation of whole emboli, we frequently observed that even as fibrin clots were being lysed and washed out early after embolization, many microvessels retained small fragments from the original clot. These fragments were also enveloped by the membrane of endothelial cells, while additional fragments seemed to have already extravasated (Supplementary Fig. 8). In contrast to extravasation of whole emboli, this phenomenon of fragment engulfment occurs in the first few days after occlusion. Thus, it is possible that smaller-scale extravasations can act synergistically with haemodynamic forces and the fibrinolytic system in the early stages of occlusion to accelerate clot dislodgment and wash-out in microvessels.

The process of envelopment and extravasation of emboli is likely to involve complex cellular and molecular events, which may include the

degradation of tight-junction proteins, adherens junctions and extracellular matrix. Matrix metalloproteinases (MMPs) have been shown to be capable of disrupting these structures[16] and have been implicated in guidance, lumen formation and barrier function in developing blood vessels[17]. We therefore investigated the role of MMPs in the extravasation process by measuring MMP-2/9 activity as reflected by tissue gelatinolytic activity, with the use of *in situ* zymography. We found prominent MMP-2/9 activity in areas immediately adjacent to emboli (Fig. 3a–c). This activity may originate from adjacent endothelial and perivascular cells such as pericytes, which have been shown to secrete MMPs[18]. To further characterize the role of MMPs in the extravasation process, we treated fibrin-clot and microsphere-embolized mice with the MMP-2/9 inhibitor SB-3CT and found a marked decrease in their extravasation (Fig. 3d, e, and Supplementary Fig. 9). Thus, MMP-2 and MMP-9 seem to be important in mediating focal proteolytic events that have a significant impact on the rate of embolus extravasation.

We subsequently addressed the impact of microvessel occlusion and recanalization on the structure and viability of blood vessels and the surrounding neurons. Microsphere embolization in 4-month-old mice led to tissue hypoxia, as detected by the pimonidazole hydrochloride technique (Hypoxyprobe). Hypoxia was limited to the endothelium and parenchyma generally less than 100 μm from the occlusion site (Fig. 4a) and disappeared after vessel recanalization. Occlusion was associated with little vascular degeneration (Fig. 4f and Supplementary Fig. 5) after embolization with 15-μm microspheres (but none with 10-μm microspheres). Although no obvious synaptic abnormalities were observed with synaptophysin immunolabelling (Fig. 4c, young), quantification of dendritic spines in mice expressing yellow fluorescent protein (YFP) in neurons showed a focal decrease in spine density that recovered as vessels re-established blood flow (Supplementary Fig. 10). Thus, sufficient redundancy exists in the cerebral microvasculature for occlusion of a single capillary or precapillary arteriole to induce only enough hypoxia to cause local transient synaptic pruning rather than cell death.

In contrast, 22-month-old mice showed significantly more persistent Hypoxyprobe labelling (Fig. 4b) and frequently developed dystrophic synapses as detected by labelling with synaptophysin (Fig. 4c, d) as well as a marked increase in caspase-3 immunoreactive perivascular cells (Fig. 4e, f). Furthermore, aged mice showed a significantly decreased rate of extravasation of emboli (Fig. 4g, h). Given that extravasation is an active process requiring remodelling of the endothelium and extracellular matrix, both age-related cellular alterations and increased basal lamina thickness and collagen deposition[19] may explain the decreased extravastion. The increased susceptibility to hypoperfusion-induced injury observed in ageing may be partly due to decreased extravasation rate coupled to a diminished efficiency in compensatory mechanisms to increase blood flow and an overall greater cellular vulnerability to hypoxia. Decreased extravasation in ageing may ultimately lead to capillary loss and reduction in vascular reserve, further augmenting the susceptibility to microvascular occlusion.

Our data describe a previously unknown mechanism of vascular plasticity that leads to the recanalization of occluded cerebral microvessels when fibrinolysis and haemodynamic forces fail (Supplementary Figs 1, 2 and 14). This mechanism is likely to be essential for clearing emboli composed of materials such as cholesterol or complex

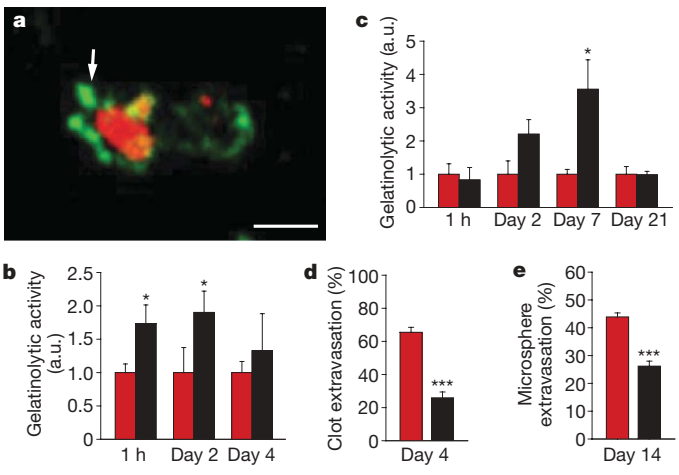

Figure 3 | MMP-2/9 activity is induced around the occlusion site. a, *In situ* zymography 5 h after embolization indicates increased gelatinolytic activity (green) around a fibrin clot (red). Scale bar, 10 μm. **b**, **c**, Quantification of gelatinolytic activity around clot-occluded (red bars in **b**), microsphere-occluded (red bars in **c**) and adjacent unoccluded (black bars in **b** and **c**) microvessels. Results are shown as means and s.e.m.; $n = 35$ mice and 110 clot-occluded vessels, and $n = 10$ mice and 75 microsphere-occluded vessels. Asterisk, $P < 0.05$, one-way analysis of variance. Black bars, unoccluded vessels. **d**, **e**, Quantification of the percentage of extravasated clots (**d**) and microspheres (**e**) in mice treated with MMP-2/9 inhibitor SB-3CT (black bars) and saline control (red bars). Results are shown as means and s.e.m.; $n = 4$ mice per treatment group. Three asterisks, $P < 0.001$, two-tailed Student's *t*-test.

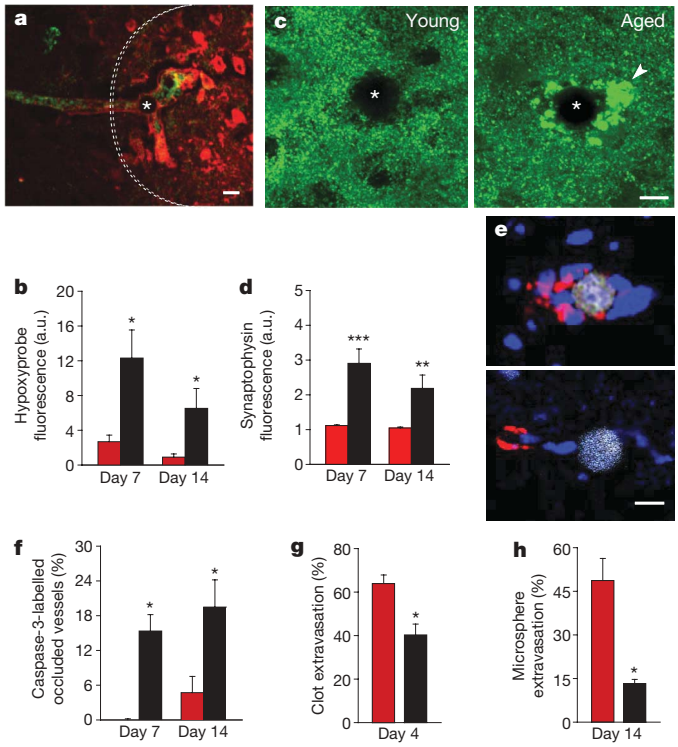

Figure 4 | Delayed extravasation in ageing contributes to persistent hypoxia, synaptic injury and cell death. a, Occlusion of a microvessel (green lectin) by a microsphere (asterisk) induced focal hypoxia (dotted area) as detected by Hypoxyprobe (red). Scale bar, 15 μm. **b**, Quantification of Hypoxyprobe around microspheres in young (red bars) and aged (black bars) mice. Results are shown as means and s.e.m.; $n = 4$ mice and 38 blood vessels per group. Asterisk, $P < 0.05$, two-tailed Student's *t*-test. **c**, Confocal images of synaptophysin immunoreactivity (green) near occlusion (asterisk) show enlarged dystrophic synapses (arrowhead) in aged mice. Scale bar, 10 μm. **d**, Quantification of synaptophysin immunoreactivity shows greater fluorescence in aged mice (black bars) than in young mice (red bars), reflecting synaptic dystrophy. Results are shown as means and s.e.m.; $n = 11$ mice and 147 blood vessels. Two asterisks, $P < 0.01$; three asterisks, $P < 0.001$; two-tailed Student's *t*-test. **e**, Occlusion by microspheres (grey) in aged mice induces caspase-3 immunoreactivity (red) in perivascular cells. The blue stain is 4,6-diamidino-2-phenylindole (DAPI). Scale bar, 10 μm. **f**, Proportion of vessels that contain caspase-3 immunoreactivity in young (red bars) and aged (black bars) mice. Results are shown as means and s.e.m.; $n = 12$ mice and 112 blood vessels. Asterisk, $P < 0.05$, two-tailed Student's *t*-test. **g**, **h**, Rate of clot (**g**) and microsphere (**h**) extravasation in young adult (red bars) and aged (black bars) mice. Results are shown as means and s.e.m.; $n = 6$ mice and 45 blood vessels for clots, and $n = 8$ mice and 2,527 blood vessels for microspheres. Asterisk, $P < 0.05$, two-tailed Student's *t*-test.

blood clots that are not susceptible to fibrinolysis; it may thus be critical for tissue reperfusion after thromboembolic stroke. This is consistent with the fact that MMP-2/9 inhibitors, which delay extravasation, have been shown to worsen outcome in stroke[20].

Although transient occlusion of large cerebral vessels is known to cause synaptic damage[21], we show that occlusion of microvessels, although affecting the blood flow of only a few branches downstream[22], can still cause sufficient hypoxia to induce transient focal dendritic spine loss (Supplementary Fig. 10). In ageing, this leads to more severe synaptic injury and perivascular cell death, which could be of special relevance given that age-related structural vascular changes[19] and decreased efficiency of the fibrinolytic system[23] may make the microvasculature prone to occlusion. Delayed extravasation could thus constitute an independent mechanism of cerebral pathology and it may also contribute to cognitive deterioration in patients with Alzheimer's disease with co-morbid conditions affecting the microvasculature such as chronic hypertension, diabetes and amyloid angiopathy[24,25].

Although a normal blood–brain barrier is essential for maintaining the chemical homeostasis of the brain, and abnormalities in the blood–brain barrier may worsen the outcome of ischaemic stroke[26] or lead to neurodegeneration[27,28], our results show that a spatially and temporally regulated mechanism of microvascular plasticity leads to a breach in the blood–brain barrier that serves an important protective role. Improvements in our understanding of this vascular mechanism could lead to therapeutic strategies aimed at preventing age-related cognitive decline and mitigating the consequences of cerebral microembolisms[29]. This mechanism may also be important for recanalization of the microvasculature outside the cerebral circulation.

METHODS SUMMARY

To induce cerebral embolization, fluorescently conjugated fibrin clots, cholesterol emboli (8–20 μm in diameter) or polystyrene microspheres (10 or 15 μm in diameter) were infused through the mouse's internal carotid artery. Emboli were imaged in fixed tissues by confocal microscopy after vessel labelling by intravenous injection of fluorescein isothiocyanate-tagged *Lycopersicon esculentum* or thioflavin-S or by immunolabelling with anti-PECAM-1, anti-collagen IV or anti-ZO-1 antibodies. Emboli were also imaged over time *in vivo* by transcranial two-photon microscopy (TPM) in mice expressing GFP in endothelial cells (Tie2–GFP and ACTB–eGFP) or wild-type mice injected intravenously with thioflavin-S. Blood flow velocity was recorded by line-scan TPM imaging to verify microvascular occlusion and re-establishment of flow. Transmission electron microscopy was performed after injection of fibrin emboli conjugated with electron dense colloidal carbon. Quantification of extravasation efficiency was performed on confocal images of fixed brain slices and in a subset of experiments from *in vivo* TPM time-lapse images. MMP-2/9 activity was measured in areas adjacent to emboli with the use of fluorescent *in situ* zymography. SB-3CT was administered for the selective inhibition of MMP-2/9 activity to determine the role of MMPs in the extravasation process. Perivascular hypoxia was detected by the administration and immunohistochemical detection of Hypoxyprobe. Dendritic spine density was quantified in confocal image stacks of fixed brain slices from mice expressing YFP in a subset of pyramidal neurons. Immunohistochemistry of synaptophysin was used for comparison of synapse puncta between adult and aged mice.

Full Methods and any associated references are available in the online version of the paper at www.nature.com/nature.

Received 4 December 2008; accepted 9 March 2010.

1. Siebler, M., Kleinschmidt, A., Sitzer, M., Steinmetz, H. & Freund, H. J. Cerebral microembolism in symptomatic and asymptomatic high-grade internal carotid artery stenosis. *Neurology* **44,** 615–618 (1994).
2. Markus, H. S., Thomson, N. D. & Brown, M. M. Asymptomatic cerebral embolic signals in symptomatic and asymptomatic carotid artery disease. *Brain* **118,** 1005–1011 (1995).
3. Vermeer, S. E. *et al.* Silent brain infarcts and the risk of dementia and cognitive decline. *N. Engl. J. Med.* **348,** 1215–1222 (2003).
4. Collen, D. On the regulation and control of fibrinolysis. Edward Kowalski Memorial Lecture. *Thromb. Haemost.* **43,** 77–89 (1980).
5. Powers, W. J., Grubb, R. L. Jr, Darriet, D. & Raichle, M. E. Cerebral blood flow and cerebral metabolic rate of oxygen requirements for cerebral function and viability in humans. *J. Cereb. Blood Flow Metab.* **5,** 600–608 (1985).
6. Levin, E. G. & del Zoppo, G. J. Localization of tissue plasminogen activator in the endothelium of a limited number of vessels. *Am. J. Pathol.* **144,** 855–861 (1994).
7. Zlokovic, B. V. *et al.* Expression of tissue plasminogen activator in cerebral capillaries: possible fibrinolytic function of the blood–brain barrier. *Neurosurgery* **37,** 955–961 (1995).
8. Rapp, J. H. *et al.* Atheroemboli to the brain: size threshold for causing acute neuronal cell death. *J. Vasc. Surg.* **32,** 68–76 (2000).
9. Grutzendler, J., Kasthuri, N. & Gan, W. B. Long-term dendritic spine stability in the adult cortex. *Nature* **420,** 812–816 (2002).
10. Muller, W. A. Leukocyte–endothelial–cell interactions in leukocyte transmigration and the inflammatory response. *Trends Immunol.* **24,** 327–334 (2003).
11. Engelhardt, B. & Wolburg, H. Mini-review: Transendothelial migration of leukocytes: through the front door or around the side of the house? *Eur. J. Immunol.* **34,** 2955–2963 (2004).
12. Dejana, E. Endothelial cell–cell junctions: happy together. *Nature Rev. Mol. Cell Biol.* **5,** 261–270 (2004).
13. Kamei, M. *et al.* Endothelial tubes assemble from intracellular vacuoles *in vivo*. *Nature* **442,** 453–456 (2006).
14. Carman, C. V. & Springer, T. A. A transmigratory cup in leukocyte diapedesis both through individual vascular endothelial cells and between them. *J. Cell Biol.* **167,** 377–388 (2004).
15. Peppiatt, C. M., Howarth, C., Mobbs, P. & Attwell, D. Bidirectional control of CNS capillary diameter by pericytes. *Nature* **443,** 700–704 (2006).
16. Yang, Y., Estrada, E. Y., Thompson, J. F., Liu, W. & Rosenberg, G. A. Matrix metalloproteinase-mediated disruption of tight junction proteins in cerebral vessels is reversed by synthetic matrix metalloproteinase inhibitor in focal ischemia in rat. *J. Cereb. Blood Flow Metab.* **27,** 697–709 (2007).
17. Stratman, A. N. *et al.* Endothelial cell lumen and vascular guidance tunnel formation requires MT1-MMP-dependent proteolysis in 3-dimensional collagen matrices. *Blood* **114,** 237–247 (2009).
18. Page-McCaw, A., Ewald, A. J. & Werb, Z. Matrix metalloproteinases and the regulation of tissue remodelling. *Nature Rev. Mol. Cell Biol.* **8,** 221–233 (2007).
19. Farkas, E. & Luiten, P. G. Cerebral microvascular pathology in aging and Alzheimer's disease. *Prog. Neurobiol.* **64,** 575–611 (2001).
20. Zhao, B. Q. *et al.* Role of matrix metalloproteinases in delayed cortical responses after stroke. *Nature Med.* **12,** 441–445 (2006).
21. Zhang, S., Boyd, J., Delaney, K. & Murphy, T. H. Rapid reversible changes in dendritic spine structure *in vivo* gated by the degree of ischemia. *J. Neurosci.* **25,** 5333–5338 (2005).
22. Nishimura, N. *et al.* Targeted insult to subsurface cortical blood vessels using ultrashort laser pulses: three models of stroke. *Nature Methods* **3,** 99–108 (2006).
23. Gleerup, G. & Winther, K. The effect of ageing on platelet function and fibrinolytic activity. *Angiology* **46,** 715–718 (1995).
24. Arvanitakis, Z., Wilson, R. S., Bienias, J. L., Evans, D. A. & Bennett, D. A. Diabetes mellitus and risk of Alzheimer disease and decline in cognitive function. *Arch. Neurol.* **61,** 661–666 (2004).
25. Iadecola, C. Neurovascular regulation in the normal brain and in Alzheimer's disease. *Nature Rev. Neurosci.* **5,** 347–360 (2004).
26. Lo, E. H., Dalkara, T. & Moskowitz, M. A. Mechanisms, challenges and opportunities in stroke. *Nature Rev. Neurosci.* **4,** 399–415 (2003).
27. Abbott, N. J., Ronnback, L. & Hansson, E. Astrocyte–endothelial interactions at the blood-brain barrier. *Nature Rev. Neurosci.* **7,** 41–53 (2006).
28. Zlokovic, B. V. The blood–brain barrier in health and chronic neurodegenerative disorders. *Neuron* **57,** 178–201 (2008).
29. Pugsley, W. *et al.* The impact of microemboli during cardiopulmonary bypass on neuropsychological functioning. *Stroke* **25,** 1393–1399 (1994).

Supplementary Information is linked to the online version of the paper at www.nature.com/nature.

Acknowledgements We thank S. Lo, C. Freitas, D. Choi and C. Whiteus for help with experiments; A. Schain for suggesting the use of ACTB–eGFP mice; E. Mugnaini for advice with transmission electron microscopy experiments; and G. D'avossa, J. García-Añoveros, J. Kessler and P. Opal for helpful discussions and critical review of the manuscript. This work was supported by National Institutes of Health/National Institute on Aging grant AG027855 (J.G.) and a Howard Hughes Medical Institute medical student research fellowship (C.K.L.).

Author Contributions J.G., C.K.L. and T.Y. conceived and designed the project. C.K.L., T.Y., B.H. and J.G. performed *in vivo* two-photon imaging. C.K.L., B.H. and J.G. adapted the technique and performed electron microscopy experiments. C.K.L. and T.Y. performed *in situ* zymography, ageing mice and SB-3CT experiments. T.Y. performed cell culture and the imaging experiment on human umbilical-vein endothelial cells. Z.L., C.K.L., T.Y., B.H. and J.G. performed histological and confocal microscopy experiments. J.G. wrote the manuscript with significant input from C.K.L. and T.Y.

Author Information Reprints and permissions information is available at www.nature.com/reprints. The authors declare no competing financial interests. Readers are welcome to comment on the online version of this article at www.nature.com/nature. Correspondence and requests for materials should be addressed to J.G. (grutzj@northwestern.edu).

METHODS

Animals. CB6F1 mice (Jackson Labs) were used for young–aged comparison studies. Tie2–GFP mice (Jackson Labs) were used for *in vivo* TPM imaging of microvessels. Thy1–YFPH mice (B6.Cg-Tg (Thy1-YFP)16Jrs/J; Jackson Labs) were used to reveal neuronal processes and quantify dendritic spines. Mice expressing GFP under the CX3CR1 chemokine receptor promoter were used for *in vivo* imaging of microglia (B6.129P(Cg)-*Ptprc*^{a} *Cx3cr1*^{tm1Litt}/LittJ; Jackson Labs). Mice expressing eGFP under the control of the chicken β-actin promoter (ACTB–eGFP; Jackson Labs) were used to reveal cells (leukocytes) flowing within microvessels. All other experiments used CD1 mice. All studies were conducted in mice between 3 and 5 months old except ageing studies, which used 22-month-old mice. Experimental protocols were approved by the Northwestern University Feinberg School of Medicine Institutional Animal Care and Use Committee.

Preparation of emboli. Heterologous fibrin-rich clots were generated by collecting blood from the left ventricle of mice with the same genetic background as the experimental ones. Mouse thrombin (10 μl of 1,000 NIH units mg^{-1}; Sigma) was added to blood immediately after extraction and incubated for 1 h at room temperature (about 20 °C). Clots were produced with and without cell lysis by rinsing with doubly distilled water. To facilitate clot production and minimize the unnecessary killing of mice, experiments requiring a larger number of animals were done with clots generated directly from fibrinogen (0.6 g ml^{-1} in 1 × PBS; cat. no. F8630; Sigma). For either method, fibrin clots were fragmented by sonication and fluorescently conjugated by incubation for 4 h with Texas Red-X succinimidyl ester (1 mg ml^{-1} in ethanol; Invitrogen). Labelled clot fragments were washed with 70% ethanol and filtered through sieves (8–20 μm pore size; Biodesign) and resuspended in 1 × PBS at predetermined concentrations to achieve sparse microvascular occlusion. For detection with transmission electron microscopy, clots were conjugated with colloidal carbon (Higgins, waterproof india ink, passed through a 200-nm filter) or 48-nm polystyrene nanoparticles (Duke Scientific) by mixing the fibrinogen solution (500 μl) with the carbon or nanoparticle suspension before thrombin administration for clot generation. Cholesterol emboli were generated by melting 100 mg of cholesterol crystals (Sigma) at 150 °C and adding Texas Red-X succinimidyl ester to label them fluorescently. The solution was crystallized at room temperature, sonicated in 1 × PBS, filtered through sieves (8–20 μm pore size) and resuspended. Microsphere emboli were prepared by diluting red fluorescent polystyrene microspheres (10 or 15 μm) (1.25×10^4 microspheres ml^{-1}; EZ-Trac; IMT/Stason) in 1 × PBS at predetermined concentrations.

Embolization surgery. Mice were anaesthetized either by intraperitoneal injection of ketamine/xylazine (120 mg ml^{-1}/10 mg ml^{-1}) or by inhalation of isoflurane. A ventral midline incision was made in the neck to gain access to the left common carotid artery (CCA). The CCA was separated from surrounding connective tissue, and blood flow was interrupted by means of retracting sutures. The left external carotid was clamped with temporary ligating sutures to divert emboli into the cerebral circulation by means of the left internal carotid artery. A small incision was made in the CCA with fine microsurgical scissors, and a custom-made catheter attached to a Hamilton syringe filled with 200 μl of solution containing emboli at the desired concentrations was inserted into the CCA. All types of emboli were infused over a roughly 2-min period. The catheter was removed and the incision was resealed with cyanoacrylate glue (Scotch). Ligating sutures were removed and CCA patency was confirmed by observation of adequate blood filling and CCA pulsations. The surgical wound was sutured and mice were carefully monitored postoperatively.

***In vivo* two-photon imaging.** Anaesthetized mice previously infused with emboli were injected through the tail vein with about 100 μl of thioflavin-S (1% in 0.5% PBS; Sigma), rhodamine-B dextran (1% in 1 × PBS; Invitrogen) or Clear Blue dye (Risk Reactor) to label the cerebral vasculature. A midline incision was made in the scalp, and an imaging window was created above the somatosensory cortex by thinning a roughly 700-μm diameter skull area with a high-speed drill (Fine Science Tools) as described previously[9], followed by skull immobilization by attachment to a stainless steel plate. Before two-photon imaging, the precise location of emboli was mapped by taking a digital image of the surface microvasculature and respective emboli under fluorescence microscopy. A two-photon microscope (Prairie Technologies) was used for *in vivo* imaging. The Ti-sapphire laser (Coherent Inc.) was tuned to 890 nm for simultaneous imaging of microvessels and emboli. Images were taken with a water-immersion objective (40×, 0.8 numerical aperture; Olympus) at a *z*-step of 1 μm and a zoom of ×1–4. Blood-flow velocity was recorded in individual cortical microvessels with line-scan imaging of flowing blood cells and fluorescent intravascular dye as described previously[30]. After imaging, the skull plate was removed and the scalp incision was closed with 6-0 (0.07 mm thickness) nylon sutures (Ethicon). The animal was placed back into its cage and monitored until the next imaging time point.

Quantification of emboli retention, washout and extravasation. Early washout (embolus retention): about 1,500 fibrin or cholesterol emboli were infused through the internal carotid artery. At 2 h after embolization, mice were killed and postfixed with 4% paraformaldehyde without cardiac perfusion to avoid perfusion-induced embolus washout. Vibratome sections (100 μm) of the brain were obtained and imaged with fluorescence microscopy. The total number of emboli in the brain was estimated by counting the number of emboli within a sample of five representative slices per animal and extrapolating the total number of emboli in the brain, taking into account the total number of slices in the forebrain. Data are reported as absolute numbers of emboli counted.

Delayed washout: mice were injected with about 1,500 fibrin or cholesterol emboli and processed in the same way as described above. Mice were killed at various time points ranging from 2 h to 6 days. The absolute number of remaining emboli was calculated at each time point and subtracted from the results obtained from the number of emboli remaining at 2 h after embolization. Washout was plotted as the percentage change over time of emboli remaining in the brain.

Extravasation: mice were embolized with fibrin, cholesterol or polystyrene emboli. Before the mice were killed, cerebral vasculature was labelled by intravenous injection of fluorescently conjugated *Lycopersicon esculentum* lectin (100 μl, 1 mg ml^{-1}; Vector Laboratories). Brain slices (50 μm) were obtained with a Vibratome and imaged with confocal microscope to quantify extravasation. Emboli were classified by whether they remained within the lumen or were outside it. The extravasation rate was calculated as the number of extravasation events divided by the total number of clots counted in all brain slices. Quantification of extravasation efficiency with the use of microspheres eliminates the potential bias caused by extravascular degradation, fibrinolysis or washout of clots and the ambiguity encountered when categorizing partly extravasated clots into extravasated or non-extravasated categories. Furthermore, microsphere size and shape are very uniform, allowing accurate comparisons between aged and young mice or pharmacologically treated mice.

Measurement of extravasation in mice injected with MMP-2/9 inhibitor. Mice embolized with either fibrin clots or microspheres were injected daily (intraperitoneally) with the selective MMP-2/9 inhibitor SB-3CT (2 mg ml^{-1} in 20% dimethylsulphoxide/doubly distilled water; Biomol). Microsphere-embolized mice were treated daily with saline or SB-3CT at 2, 10 and 20 mg kg^{-1} per day or acutely with 40 mg kg^{-1}. Clot-embolized mice were given saline or SB-3CT at 20 mg kg^{-1} per day. Mice were killed 4 days after embolization for clots and 14 days after embolization for microspheres because of their different time courses of extravasation.

***In situ* zymography.** Brains were harvested at various intervals after embolization with clots or microspheres and frozen rapidly without fixation. Tissues were cryosectioned (slices 20 μm thick) and embedded in fluorescein-conjugated DQ gelatin from pig skin (15 mg ml^{-1}; Invitrogen) for 15 min at 4 °C and then for 5 h at 25 °C. Tissues were then rinsed with PBS and fixed with 4% paraformaldehyde followed by confocal imaging and fluorescence quantification.

Immunohistochemical labelling. Brain tissue was extracted after perfusion and postfixed with 4% paraformaldehyde in 1 × PBS, cryosectioned, and blocked with 3% normal goat serum/0.1% Triton X-100. Incubation with primary antibodies was performed overnight at 4 °C. The primary antibodies used were collagen IV (Abcam), BrdU (AbD Serotec), NG2 chondroitin (Chemicon), Hypoxyprobe (Chemicon), ZO-1 (Invitrogen), synaptophysin (Chemicon), CD31(PECAM-1) (BD Pharmingen), and IBA1 (Wako). For hypoxia detection, Hypoxyprobe (60 mg kg^{-1}; Chemicon) was injected intraperitoneally into embolized mice 2 h before they were killed. To detect cell proliferation, BrdU (40 mg kg^{-1}; Sigma-Aldrich) was injected intraperitoneally every 24 h after embolization until killing.

Fluorescence quantification. ZO-1, NG2, Hypoxyprobe and *in situ* zymography fluorescence were quantified from confocal images of brain slices from embolized mice. A region of interest of fixed size was centred on the embolus. The average greyscale intensity within this region of interest was calculated with NIH Image J software and normalized to fluorescence intensity in multiple control areas measured in adjacent non-occluded microvessels of equal diameter present within the same confocal optical plane. This normalization procedure controls for immunolabelling variability between animals and changes in fluorescence intensity due to different imaging depths within a confocal stack. Because images in different samples were acquired with exactly the same confocal parameters of gain, laser intensity and pinhole and the data were computed as the ratio between the region of interest and control areas within the same optical plane, this allows comparison of the ratios rather than absolute fluorescence values between different samples.

Dendritic spine quantification. Thy1–YFPH mice were embolized with 15 μm microspheres and killed at different time points after embolization (5 min, day 1, day 7 and day 42). Before the mice were killed, the intravascular dye thioflavin-S was injected. Confocal imaging of YFP-expressing dendrites in the immediate

vicinity of occluded vessels was obtained. Dendrites were segmented into three equal portions: area 1 was the intersection between the dendrite and the downstream unperfused portion of the vessel (as determined by reduced intravascular fluorescence); areas 2 and 3 served as internal controls and were, respectively, the distal and proximal segments of the dendrite to area 1. Spine density was quantified from confocal stacks and normalized by using the following formula:

$$\text{normalized spine density} = (\text{density of area 1})/0.5 \times (\text{density of area 2} + \text{density of area 3})$$

Electron microscopy. Mice were perfused with a solution of 4% paraformaldeyde and 1% glutaraldehyde 7–12 days after embolization with 10-μm microspheres or 4–8 days after embolization with fibrin clots conjugated to Texas Red-X ester (Invitrogen) as well as 48-nm nanoparticles or colloidal carbon (as described above). Coronal brain Vibratome (Leica) sections (35 μm) were generated. Diaminobenzidine (0.06% in a 5% 0.05 M Tris-HCl buffer pH 7.6; Sigma) was used to photoconvert the fluorescent clots (irradiated at a wavelength of 480 nm with a 120-V mercury lamp). The photoconverted dark clots were located under a dissecting microscope and microdissected with the tip of a 30-gauge needle into roughly 200 μm diameter pieces containing the occluded vessel. The tissue was processed for electron microscopy by standard methods. In brief, tissues were immersed in 1% osmium tetroxide for 1 h at room temperature, then dehydrated in an increasing concentration gradient of ethanol. Once fully dehydrated, tissue was transitioned in propylene oxide before transfer into EMBED-812 (Electron Microscopy Sciences) overnight. The tissues were placed in an oven at 60 °C for 24 h for polymerization. Embedded tissues were then placed on preformed epoxy blocks with a drop of resin and placed back in the oven for a further 24 h. Sections 70 nm thick were cut on a microtome (Leica), placed on copper grids and left to dry for 24 h at room temperature. Contrast enhancement was achieved by placing the grids on a 4% uranyl acetate solution for 10 min followed by 10 min in Reynold's lead citrate. With the use of a Jeol 1220 80-kV transmission electron microscope, copper grids were thoroughly scanned to locate the emboli of interest.

Human vascular endothelial cell culture and live imaging. HUVEC cells (courtesy of W. Muller) were grown on 60-mm poly(D-lysine)-treated glass-bottomed plates in Medium 200 (Invitrogen). Cells were labelled fluorescently by transduction with an adeno-associated virus driving the expression of GFP under a cytomegalovirus promoter (courtesy of J. Kessler). At 24 h after the addition of virus, the culture medium was replaced and cells were grown to confluence. Texas-Red-conjugated fibrin clots (200 μl, 5,000 clots ml^{-1}, diameter 8–20 μm) were added to the plate and left to settle for 15 min. The plates were kept at 37 °C on a heating plate and imaged every 15 min for 6 h with two-photon microscopy.

Statistical analysis. All statistical parameters were calculated with Sigma Plot software. Student's *t*-test was used for most data analysis. For comparison between more than two groups, an analysis of variance test was used. A Mann–Whitney test was used for comparing the distribution of relative fluorescence intensities of ZO-1 images. $P < 0.05$ was considered to be statistically significant.

30. Kleinfeld, D., Mitra, P. P., Helmchen, F. & Denk, W. Fluctuations and stimulus-induced changes in blood flow observed in individual capillaries in layers 2 through 4 of rat neocortex. *Proc. Natl Acad. Sci. USA* **95,** 15741–15746 (1998).